

FULL PAPER

Open Access



3D inversion of full gravity gradient tensor data in spherical coordinate system using local north-oriented frame

Yi Zhang¹, Yulong Wu^{1*}, Jianguo Yan², Haoran Wang^{3,4}, J. Alexis P. Rodriguez⁵ and Yue Qiu⁶

Abstract

In this paper, we propose an inverse method for full gravity gradient tensor data in the spherical coordinate system. As opposed to the traditional gravity inversion in the Cartesian coordinate system, our proposed method takes the curvature of the Earth, the Moon, or other planets into account, using tesseroid bodies to produce gravity gradient effects in forward modeling. We used both synthetic and observed datasets to test the stability and validity of the proposed method. Our results using synthetic gravity data show that our new method predicts the depth of the density anomalous body efficiently and accurately. Using observed gravity data for the Mare Smythii area on the moon, the density distribution of the crust in this area reveals its geological structure. These results validate the proposed method and potential application for large area data inversion of planetary geological structures.

Keywords: Gravity gradient tensor, Inversion, Density distribution, Spherical coordinate system, Local north-oriented frame

Introduction

The gravity gradient tensor (GGT) is the second derivative of the gravity potential. Compared to the general gravity field T_z , GGT contains nine components and has much higher resolution in inverting the spatial position of target anomaly bodies, which means it will offer more information to better understand the interior structure of the earth or some other planets (Li 2001; Bouman et al. 2016).

In 1886, a torsion balance gradiometer was first developed by Lorand Eotvos, becoming a useful tool for mining and hydrocarbon exploration (Pedersen and Rasmussen 1990; Bell and Hansen 1998). 3D inversion of GGT data was originally introduced by Vasco (1989) and Vasco and Taylor (1991), who focused on the covariance and resolution measures of the solution appraisal. More recently, several algorithms were developed to inverse GGT data (e.g., Li 2001; Zhdanov et al. 2004; Uieda and

Barbosa 2012; Oliveira and Barbosa 2013; Martinez et al. 2012; Geng et al. 2015; Meng 2016). The differences among these algorithms are related to the choice of model object functions in the inversion procedure; all the model object functions can be retraced back to the inversion methods used in the inversion of the general gravity field (e.g., Last and Kubik 1983; Guillen and Menichetti 1984; Barbosa and Silva 1994; Li and Oldenburg 1996, 1998; Farquharson 2008).

In addition to the choice of model object functions, there is little agreement on best component of GGT for the inversion. Li (2001) combined five independent components excluding T_{zz} . Zhdanov et al. (2004) used the horizontal components T_{xy} and $T_{uv} = (T_{xx} - T_{yy})/2$. Martinez et al. (2012) combined the horizontal components and T_{zz} . Capriotti et al. (2015) employed a combination of the GGT and general gravity field T_z . Pilkington (2012) used an eigenvalue spectra method to evaluate the utility of combining different GGT components, preferring the T_{zz} component, indicating that the source-model information is improved by adding more components only at close distance to the anomaly sources. Later, Pilkington (2013) used estimated parameter errors from parametric

*Correspondence: yunlongwu@gmail.com

¹ Key Laboratory of Earthquake Geodesy, Institute of Seismology, China Earthquake Administration, 48 Hongshan Side Road, Wuhan 430071, Hubei, China

Full list of author information is available at the end of the article

inversions, concluding that the T_{zz} component gave the best performance, while the horizontal components T_{xx} and T_{yy} performed poorly. Paoletti et al. (2016) used a singular value decomposition (SVD) tool to analyze both synthetic data and gradiometer measurements. This research showed that the main factors controlling the reliability of the inversion are algebraic ambiguity (the difference between the number of unknowns and the number of available data points) and signal-to-noise ratio.

All these inversion methods mentioned are implemented in the Cartesian coordinate system (CCS). For small-scale problems such as mining or hydrocarbon exploration on earth, the target area is usually relatively small compared to the radius of the earth and can be considered as a flat surface, so inversion in CCS works fine and obtains reliable inversion results with high accuracy. However, for large-scale inversion problems, such as density imaging of the lunar mascon with the satellite gravity datasets, the target area of the lunar mascon was usually large and covered an area with hundreds or thousands of kilometers in both longitude and latitude directions. Moreover, the radius of the moon was relatively small (1738 km), and this meant the inversion area of the mascon was no longer a flat area; hence, inversion methods cannot ignore the influences of the lunar curvature. To deal with this problem, the inversion method in the SCS must be considered. Liang et al. (2014) extended Li and Oldenburg's (1996, 1998) inversion method to the SCS using the general gravity field.

In the history of the Moon exploration, one of the most amazing discoveries was the concentrated areas of mass found on the near side of the moon (Muller and Sjogren 1968; Melosh et al. 2013; Freed et al. 2014). These concentrated areas of mass, referred to as mascons, usually have a positive gravity anomaly peak and surrounded by negative gravity anomalies with low geographical elevation. The knowledge of the interior density structure of mascons will help to understand its origin mechanism (Wang et al. 2015; Jansen et al. 2017). There has a significant improvement on lunar gravity field model development (Matsumoto et al. 2010; Yan et al. 2012), and the recent high solution gravity field model GL1500E derived from GRAIL mission (The Planetary Data System 2016) makes it possible to investigate the interior density structure of the mascons (Zuber et al. 2013a, b) using lunar gradient data.

The high-resolution lunar gradient data produced from GRAIL gravity was applied by Andrews-Hanna et al. (2014) to investigate the structure and evolution of the lunar Procellarum region. The fault geometry, thermal structure, and material content were considered to generate rectilinear patterns of the gradient data in this region.

A forward modeling method coupling with finite element method (FEM) was employed this work. GGT is the difference of gravity in different directions, which helps to remove the influence of the long-wave part in the lunar gravity, and it is easier to highlight the lunar gravity's shortwave effect and to get a better resolution for density imaging. In this work, we will focus on inversion of the lunar gradient data, which is different from the previous work (Andrews-Hanna et al. 2013).

The remainder of this paper is as follows: a brief introduction of this inversion method is presented in second section. Third section details two different models and experiments with synthetic GGT datasets and inversion of GGT observation datasets of moon. The interior density structure of the Mare Smythii mascon is discussed in fourth section. Finally, in fifth section we present the conclusions of this study.

Methodology

GGT in the spherical coordinate system

The two most commonly used frames in SCS are the geocentric spherical frame (GSF) and the local north-oriented frame (LNOF). The GGT is expressed in terms of the second derivatives of the gravitational potential U in the r , λ , and φ directions of GSF, where r , λ , and φ refer to the radial, longitude, and latitude, respectively (Eq. 1).

$$T = \begin{bmatrix} T_{\lambda\lambda} & T_{\lambda\varphi} & T_{\lambda r} \\ T_{\varphi\lambda} & T_{\varphi\varphi} & T_{\varphi r} \\ T_{r\lambda} & T_{r\varphi} & T_{rr} \end{bmatrix} = \begin{bmatrix} \frac{\partial^2 U}{r^2 \cos^2 \varphi \partial \lambda^2} & \frac{\partial^2 U}{r^2 \cos \varphi \partial \lambda \partial \varphi} & \frac{\partial^2 U}{r \cos \varphi \partial \lambda \partial r} \\ \frac{\partial^2 U}{r^2 \cos \varphi \partial \lambda \partial \varphi} & \frac{\partial^2 U}{r^2 \partial \varphi^2} & \frac{\partial^2 U}{r \partial \varphi \partial r} \\ \frac{\partial^2 U}{r \cos \varphi \partial \lambda \partial r} & \frac{\partial^2 U}{r \partial \varphi \partial r} & \frac{\partial^2 U}{\partial r^2} \end{bmatrix} \quad (1)$$

In LNOF, where z has the geocentric radial downward direction, x points to the north, and y is directed to the east with a right-handed system, relationship between the LNOF and GSF can be described as in Eq. (2) (Reed 1973; Petrovskaya and Vershkov 2006).

$$\begin{aligned} T_{xx} &= \frac{1}{r} T_r + \frac{1}{r^2} T_{\varphi\varphi} \\ T_{xy} &= \frac{1}{r^2 \cos \varphi} T_{\lambda\varphi} + \frac{\sin \varphi}{r^2 \cos^2 \varphi} T_{\lambda} \\ T_{xz} &= \frac{1}{r^2} T_{\varphi} - \frac{1}{r} T_{r\varphi} \\ T_{yy} &= \frac{1}{r} T_r + \frac{1}{r^2 \cot \varphi} T_{\varphi} + \frac{1}{r^2 \cos^2 \varphi} T_{\lambda\lambda} \\ T_{yz} &= \frac{1}{r^2 \cos \varphi} T_{\lambda} - \frac{1}{r \cos \varphi} T_{r\lambda} \\ T_{zz} &= T_{rr} \end{aligned} \quad (2)$$

In this paper, we choose to use LNOF, which will not be singular when calculating GGT components from a gravity spherical harmonics model (Eshagh 2008, 2010) and because the GGT is symmetric and the trace of the

GGT equals zero; hence, there are only five independent components.

Forward modeling

Theoretically, forward modeling is the basis of the inversion, as it forms the relationship between the model and data space. The forward modeling method we use here was developed by Asgharzadeh et al. (2007) for calculating a gravity field and its gradients in the SCS with LNOF. This method makes use of the Gauss–Legendre quadrature integration for numerically modeling theoretical gravity effects caused by the tesseroids (Anderson 1976; Heck and Seitz 2006) (Fig. 1).

According to Asgharzadeh et al. (2007), each component of the GGT can form its own relationship between the model and dataset and can be described as:

$$T_{ij} = G_{ij}m \quad i, j = x, y, z \quad (3)$$

In Eq. (3), m and G_{ij} refer to the model and kernel matrix, respectively.

To make full use of the GGT dataset, we adopt the new kernel function G as the linear combination of the five independent components of GGT:

$$G_s = \sum_{i,j}^{x,y,z} (k_{ij}G_{ij}) \quad (4)$$

k_{ij} here refers to the weighting factor of each component, and it can be considered as the data accuracies (or the reliabilities) of each component.

Due to the relationship of $T_{xx} + T_{yy} + T_{zz} = 0$, the linear combination of the components T_{xx} and T_{yy} can be described by the vertical components T_{zz} ; hence, we do not employ the components T_{xx} and T_{yy} in Eq. (4).

Similarly, the GGT dataset d_s can be also adopted into the linear combination of the independent components:

$$d_s = T_s = \sum_{i,j}^{x,y,z} (k_{ij}T_{ij}) \quad (5)$$

For each independent component T_{ij} , the error standard deviation is σ_{ij} . According to error theory, the error standard deviation of the GGT will be:

$$\sigma = \sqrt{\sum_{i,j}^{x,y,z} (k_{ij}\sigma_{ij})^2 + Cov} \quad (6)$$

In Eq. (6), Cov represents the sum of the error covariance of all components. On the assumption that the error of the GGT follows the Gaussian random distribution and one independent component has no connection with each other, then $Cov = 0$.

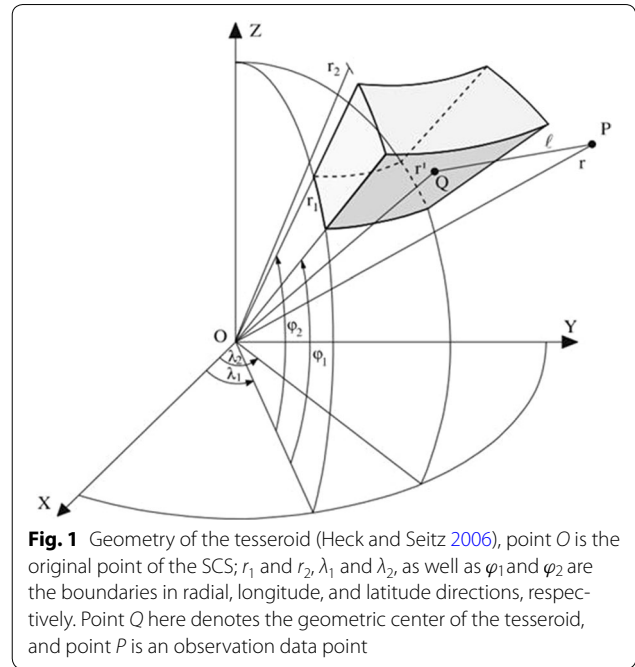


Fig. 1 Geometry of the tesseroid (Heck and Seitz 2006), point O is the original point of the SCS; r_1 and r_2 , λ_1 and λ_2 , as well as φ_1 and φ_2 are the boundaries in radial, longitude, and latitude directions, respectively. Point Q here denotes the geometric center of the tesseroid, and point P is an observation data point

Inversion method

In general, because of an insufficient observed dataset, the multiple solutions problem becomes a serious issue for the 3D gravity inversion. To deal with the problem, a suitable model objective function is required.

Li and Oldenburg (1996) and Li (2001) designed a model objective function with a maximum smoothing method; however, this model objective function is only suitable for CCS. Liang et al. (2014) extended it to the SCS using the spherical derivative operators:

$$\begin{aligned} \phi_m(m) = & \alpha_s \int_V [w(r)(m - m_{ref})]^2 dv \\ & + \alpha_r \int_V \left[\frac{\partial w(r)(m - m_{ref})}{\partial r} \right]^2 dv \\ & + \alpha_\varphi \int_V \left[\frac{\partial w(r)(m - m_{ref})}{r \partial \varphi} \right]^2 dv \\ & + \alpha_\lambda \int_V \left[\frac{\partial w(r)(m - m_{ref})}{r \cos \varphi \partial \lambda} \right]^2 dv \end{aligned} \quad (7)$$

The model object function of Eq. (7), also called stabilized function, was initially introduced by Backus and Gilbert (1967, 1968, 1970) to solve ill-posed inverse problems. It can be divided into two parts: the first item of Eq. (7) is the smallest model between recovered and reference model, and the last three items are the smoothest model between recovered and reference model in

Table 1 3D mesh and dataset for inversion

Direction	Inversion range	Model		Data	
		Grid size	Grid number	Data size	Data number
Longitude	30.0°–40.0°	0.25°	40	0.25°	41
Latitude	30.0°–40.0°	0.25°	40	0.25°	41
Depth/elevation	0–100 km	5 km	20	0.5 km	

longitudinal, latitudinal, and radial directions, respectively. In Eq. (7), m and m_{ref} refer to the recovered and reference model, respectively. α_i ($i=s, r, \lambda, \varphi$) are length scales, which control the balance of the smoothness versus smallness for the whole model, α_s for smallness, and $\alpha_r, \alpha_\lambda,$ and α_φ for smoothness (Oldenburg and Li 2005; Williams 2008). In practice, α_s usually can be assigned to a value of 1.0 or other suitable value; however, different to those in CCS (Williams 2008), $\alpha_\lambda,$ and α_φ are variable because of the different tesseroid body sizes along the radial direction. $w(r)$ here represents the depth weighting function, and it can be used to avoid the skin effect in the inversion (Li and Oldenburg 1996; Li 2001). The depth weighting functions match the decay of the gravity or magnetic kernel functions, and they are in proportion to $1/r^2$ in gravity and $1/r^3$ in magnetic inversion problem. Without them, the inversion will get results concentrated on the surface of the target area (Li 2001). Unlike the uniform prism cells in CCS, the tesseroid cells become smaller along the radial direction from surface to the core, so it must rescale them into the same level. Liang's et al. (2014) main contribution is the modification of the depth weighting function in SCS by rescaling the cell volume to the surface (see Additional file 1).

$$w^2(r) = \frac{r^2}{r_0^2(H + R - r)^2} \quad (8)$$

In Eq. (8), R is the radius of the reference sphere and H is the average height of observed dataset above the reference sphere, while r_0 and r are the radial distance of the surface and for computing tesseroid cells, respectively.

In addition, geological and geophysical constraints play an important role in the gravity inversion. The geological and geophysical constraints are varied, and they can be classified into two different kinds: (1) geometry constraints like structure boundaries, orientations, and locations information; (2) physical property constraints such as surface material content and information from drill holes. All these constraints can be described as the function of the physical property and positions. In our inversion method, as we divided the subspace into different tesseroid cells, the constraints become the function of

the physical property and index number of the tesseroid cells.

Different from the model objective function, which aims to solve the non-uniqueness in ill-posed inverse problems, the purpose of using a prior geological and geophysical information during the inversion is to improve the inversion result. In this paper, we use the Lagrangian multipliers method, introduced by Zhang et al. (2015), to fit for the different prior geological or geophysical information during the inversion procedure; the additional penalty function of the density bound constraints makes the recovered model more reliable.

Examples of synthetic GGT data

In this section, we will give two examples of the artificial synthetic model used to validate our inversion method.

Single model

Table 1 shows the 3D mesh and dataset setting for inversion. The reference radius we use is 1738 km, which is the same as the mean radius of the moon.

The artificial synthetic model we use here is a horizontal spherical prism body with constant residual density of 0.5 g/cm^3 and covers an area of $33^\circ\text{--}37^\circ$ in both the longitude and latitude directions as well as 1648–1698 km in radial direction. The background density was set to 0 g/cm^3 . Figure 2 shows the horizontal slice and vertical profile of the artificial synthetic model used for inversion.

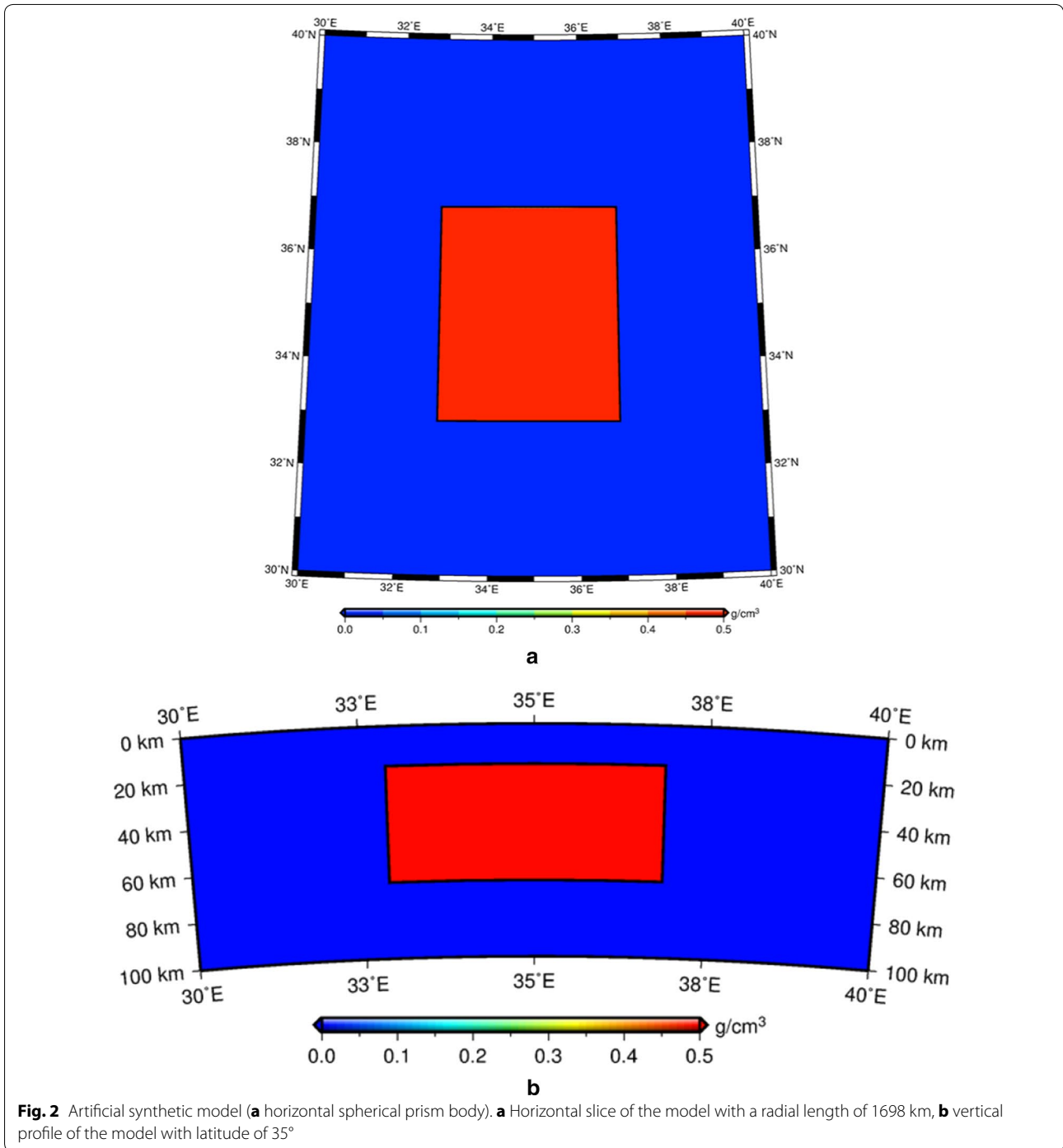
In Figs. 3, 4, we showed the artificial theoretical datasets for all the components of the GGT. Considering the geometric relationships between the model mesh and the data grids in Table 1, we also obtained the kernel matrixes $G_s = G_{xy} + G_{xz} + G_{yz} + G_{zz}$ and the GGT dataset $d_s = d_{xy} + d_{xz} + d_{yz} + d_{zz}$, as shown in Fig. 4c.

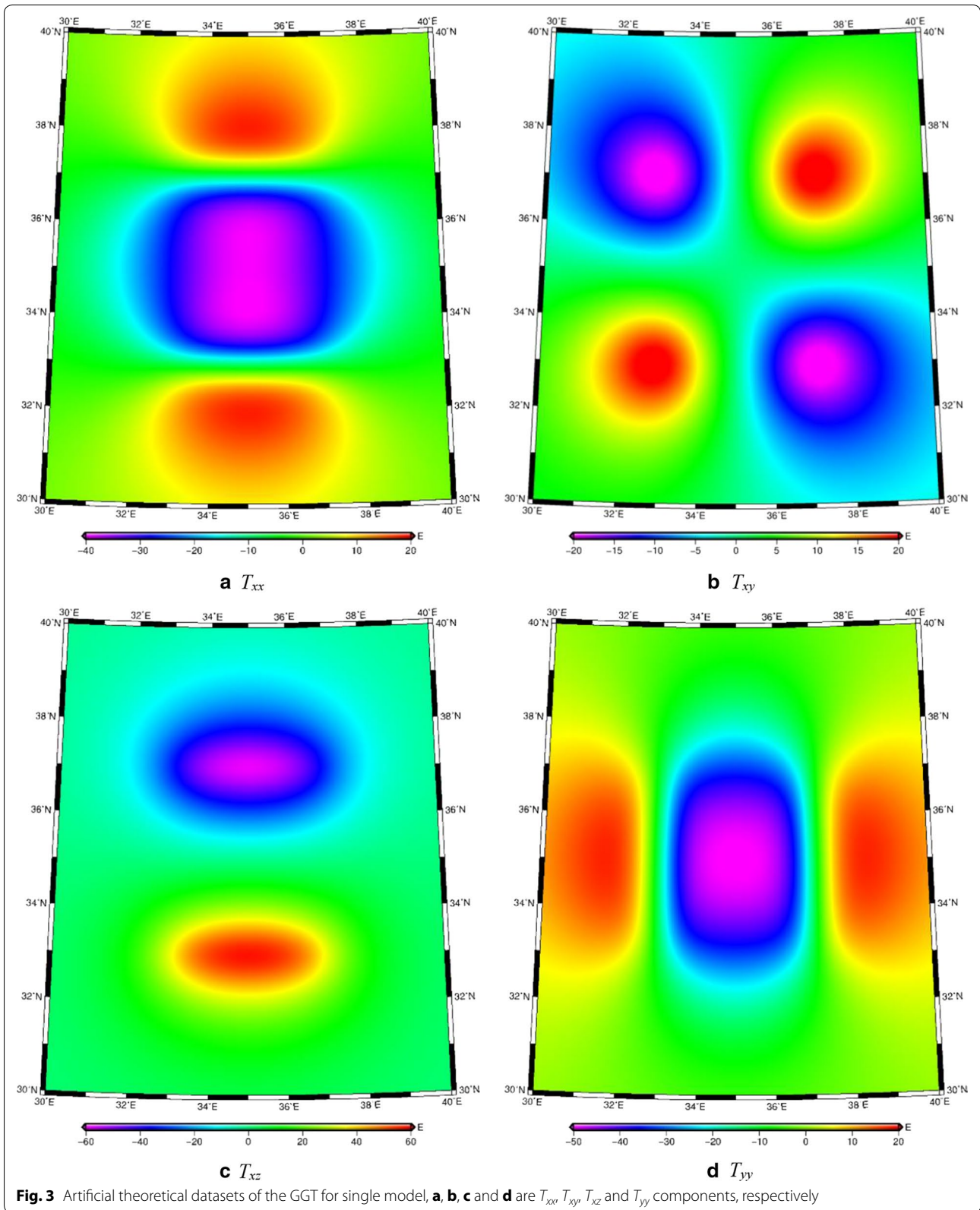
Furthermore, independent Gaussian random noise was added to each component of the GGT dataset. The mean value of the Gaussian noise was zero, the standard deviation was approximately 1% of the difference between the maximum and minimum value of each component, and the artificial theoretical datasets with noise are shown in Figs. 5, 6.

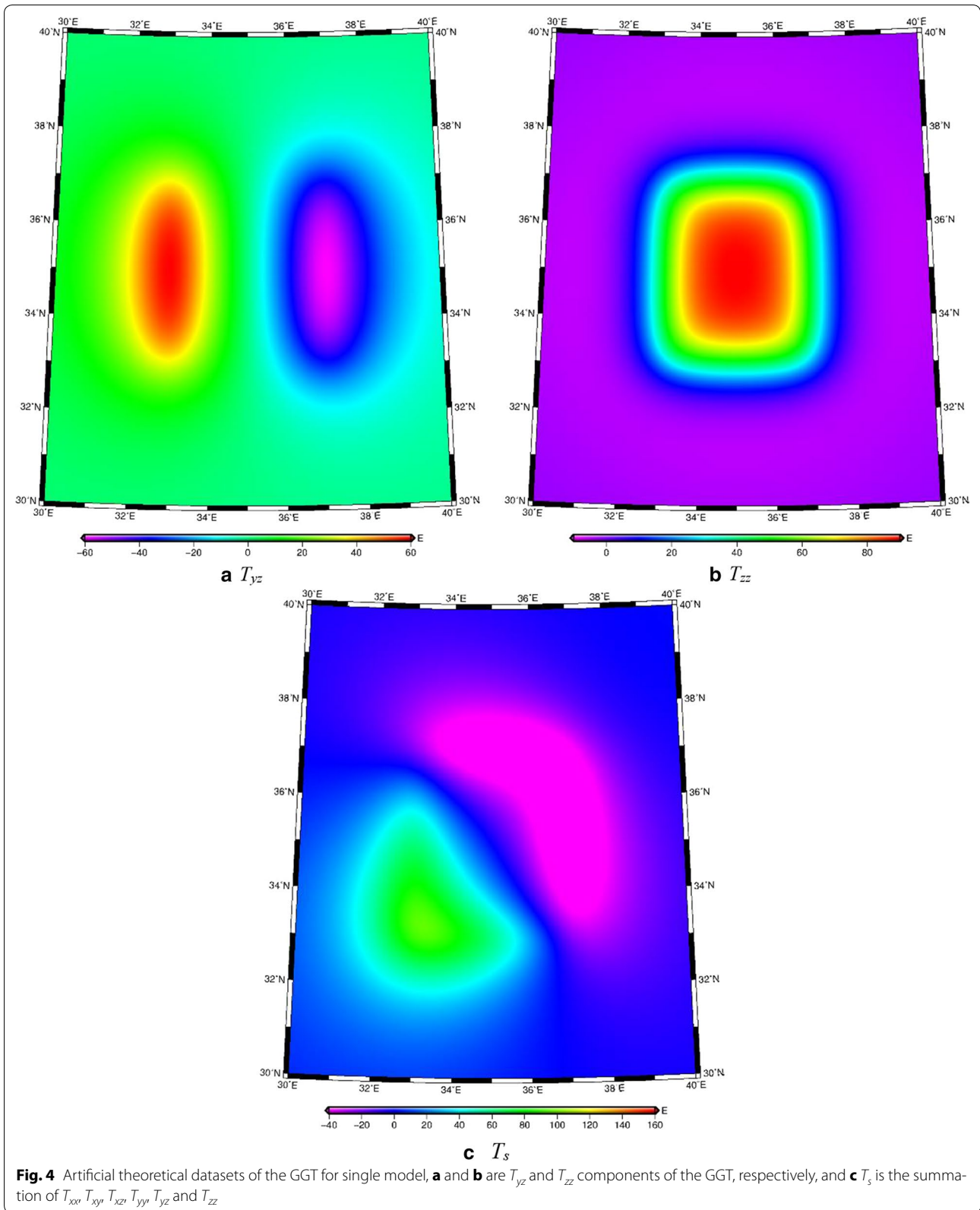
In the inversion, we assigned a density constraint between 0 and 0.5 g/cm^3 to each inverted cell. The L-curve method (Calvetti et al. 2000) was used to search

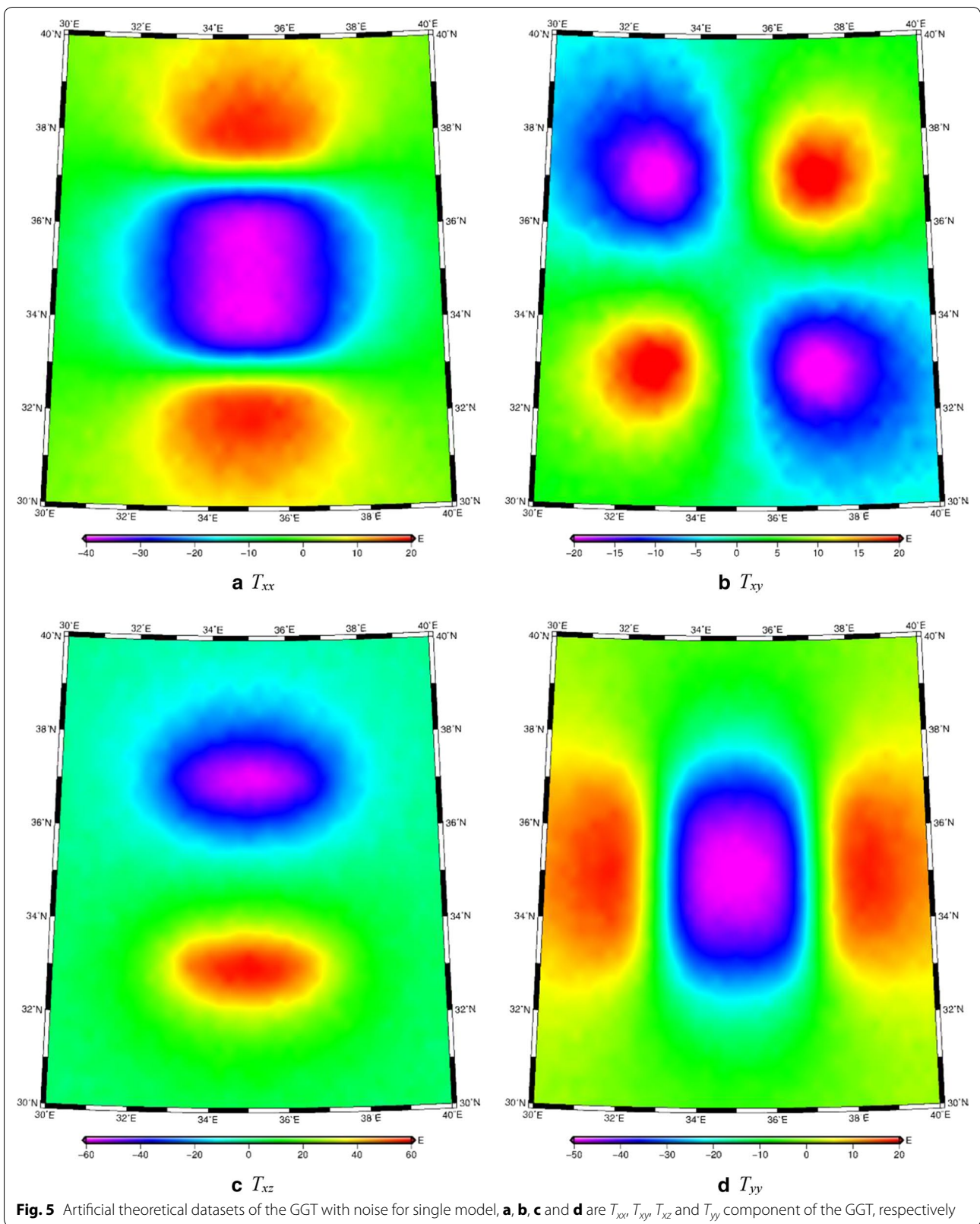
for the best Tikhonov regularization parameter (Tikhonov and Arsenin 1977), and the recovered model is shown in Fig. 7. Tikhonov regularization parameter here is the trade-off between the model objective function and data objective function (also named data misfit). The Tikhonov regularization parameter we chose is 10, which is located at the corner of L-curve, but slightly offset to the right with a smaller data misfit (Zhang et al. 2015). The

black lines in Fig. 7 indicate the boundary of the artificial synthetic model, and the recovered model was fitted well. The recovered model with minimum-structure inversions using L_2 -norm measures usually has blurred boundaries, and if sharp boundaries and blocky features are needed, the non- L_2 inversions may provide an alternative method (Sun and Li 2014).









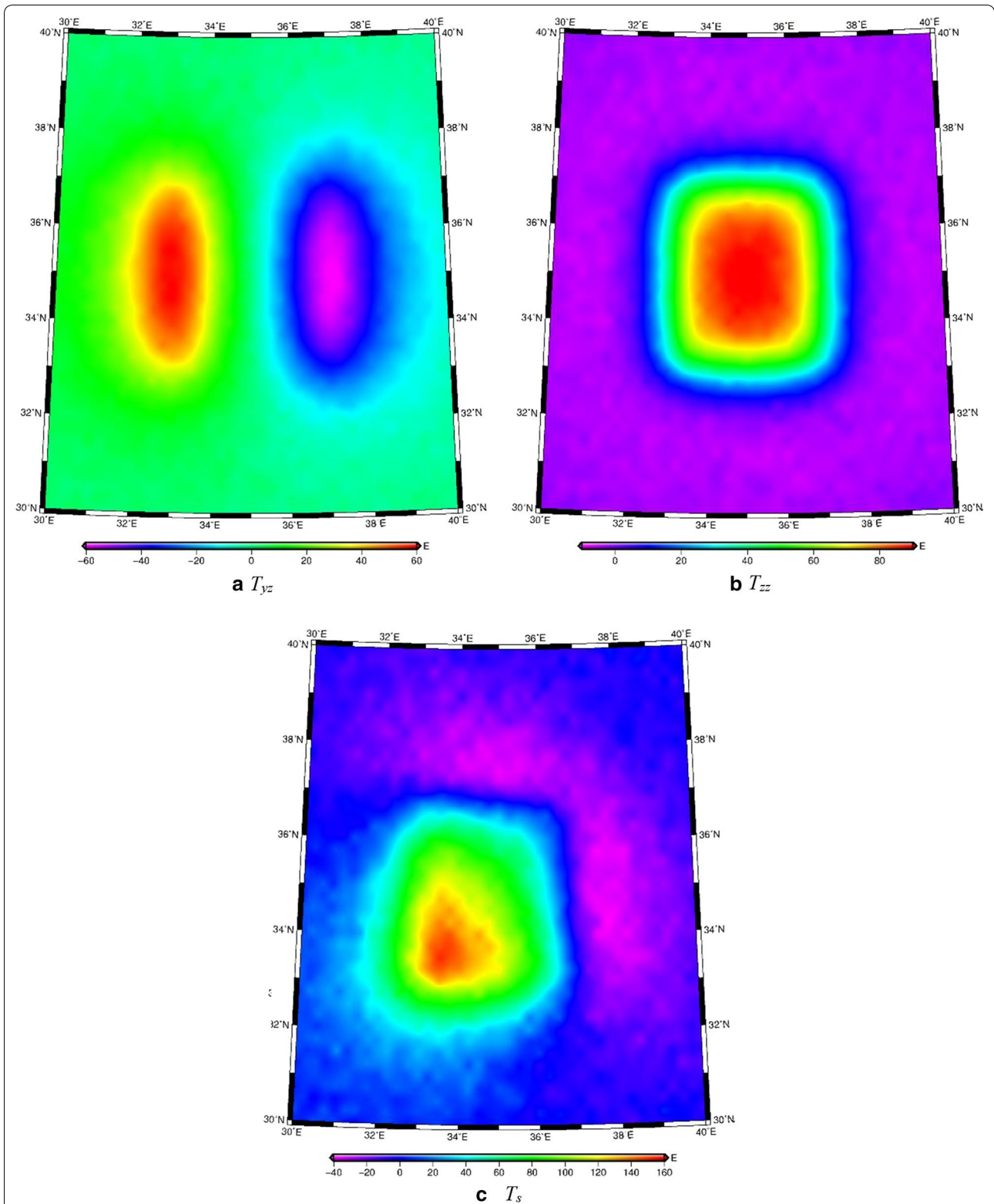
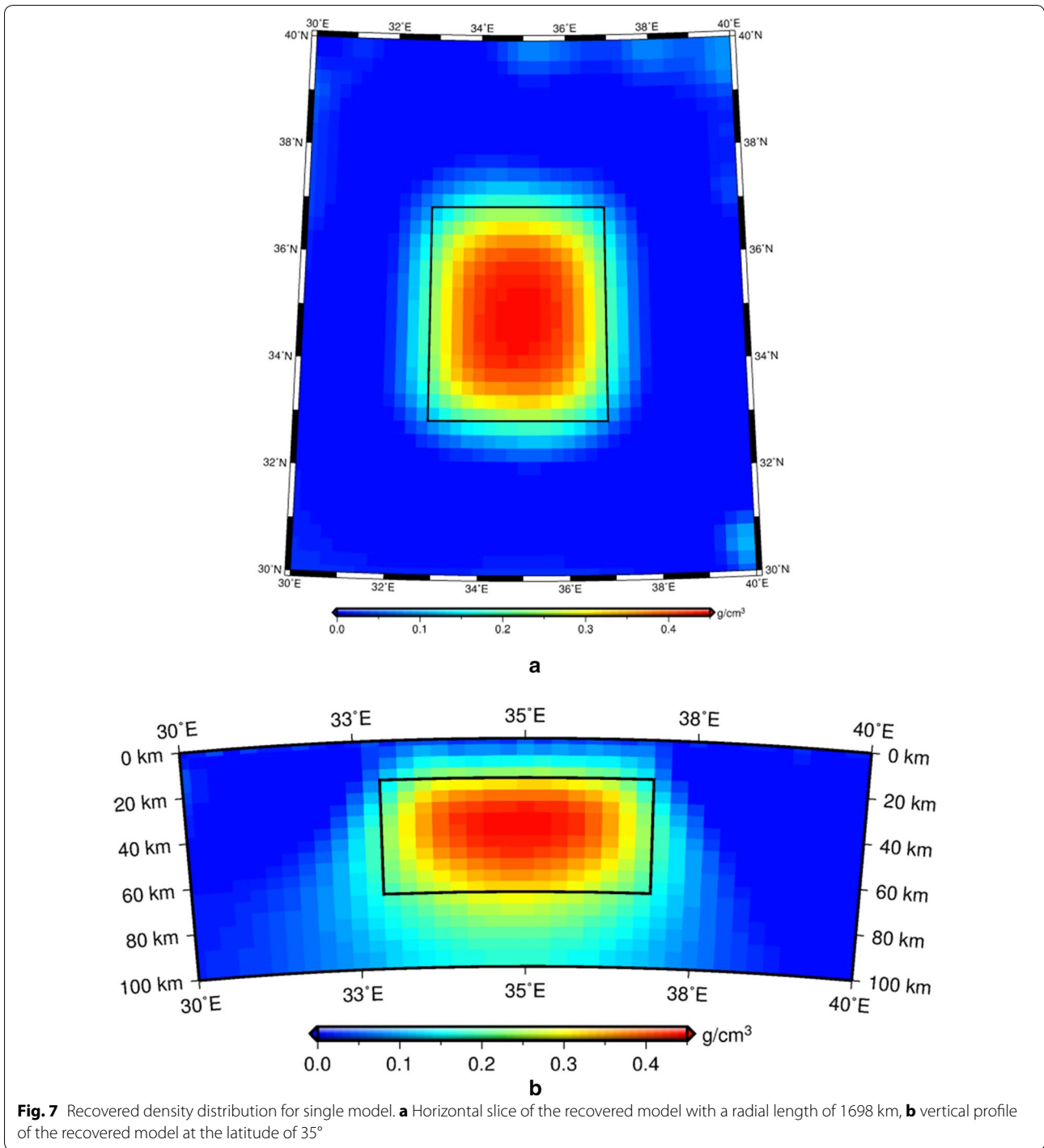


Fig. 6 Artificial theoretical datasets of the GGT with noise for single model, **a** and **b** are T_{yz} and T_{zz} components of the GGT, respectively, and **c** T_s is the summation of T_{xx} , T_{yy} , T_{zz} , T_{xy} , T_{yz} and T_{zx}



Composite models

Here we designed two composite models. One model covered an area of 34°–36°, 32°–34°, and 1678–1718 km in latitude and longitude as well as radial direction, respectively, with a small residual density of 0.2 g/cm³. The residual density of the other model was 0.7 g/cm³,

and its geological setting was 34°–36°, 36°–38°, and 1658–1698 km in latitude and longitude as well as radial direction, respectively. The 3D mesh and dataset settings we used are shown in Table 1. The horizontal slice and vertical profile of the artificial synthetic models are shown in Fig. 8.

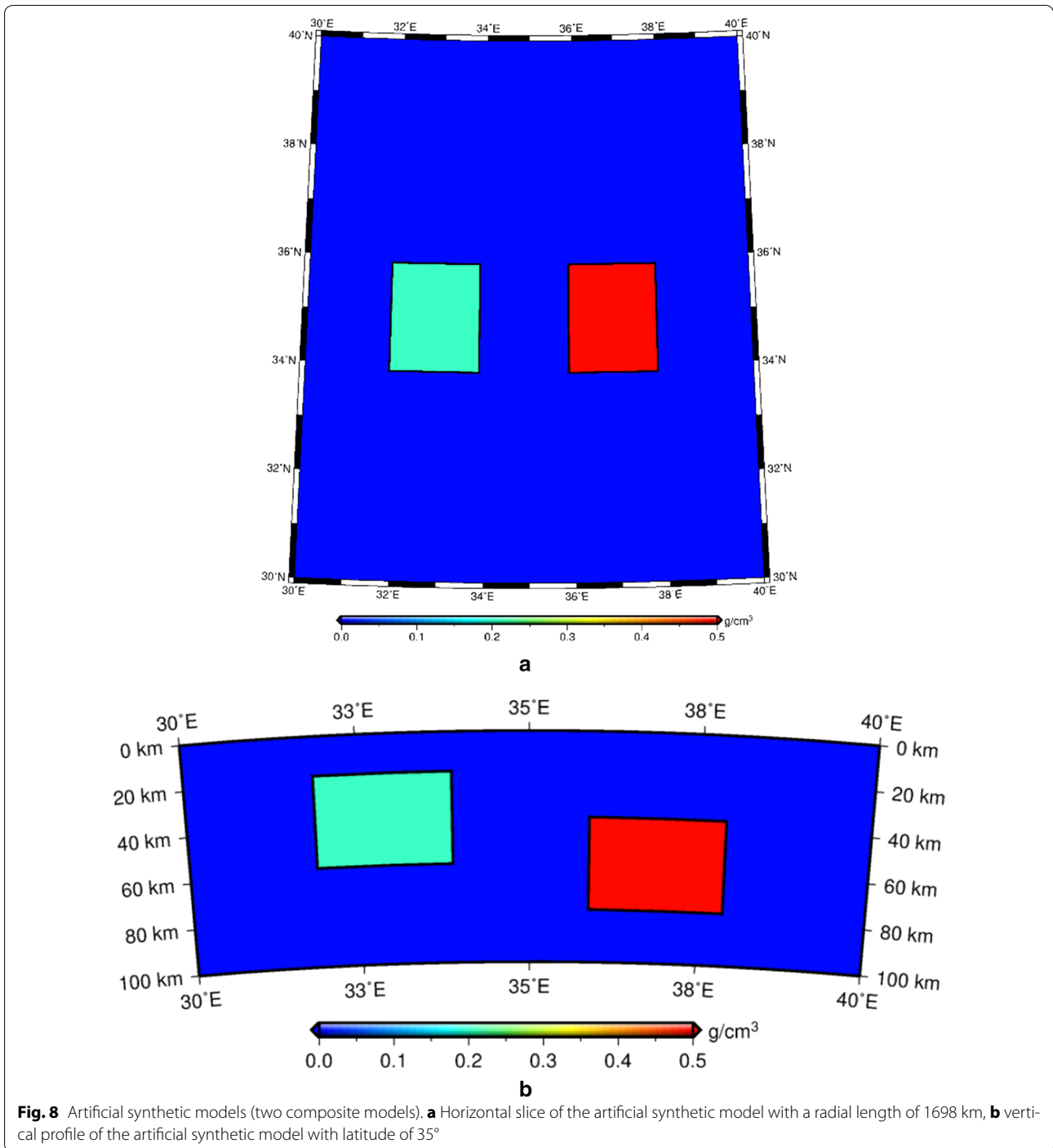


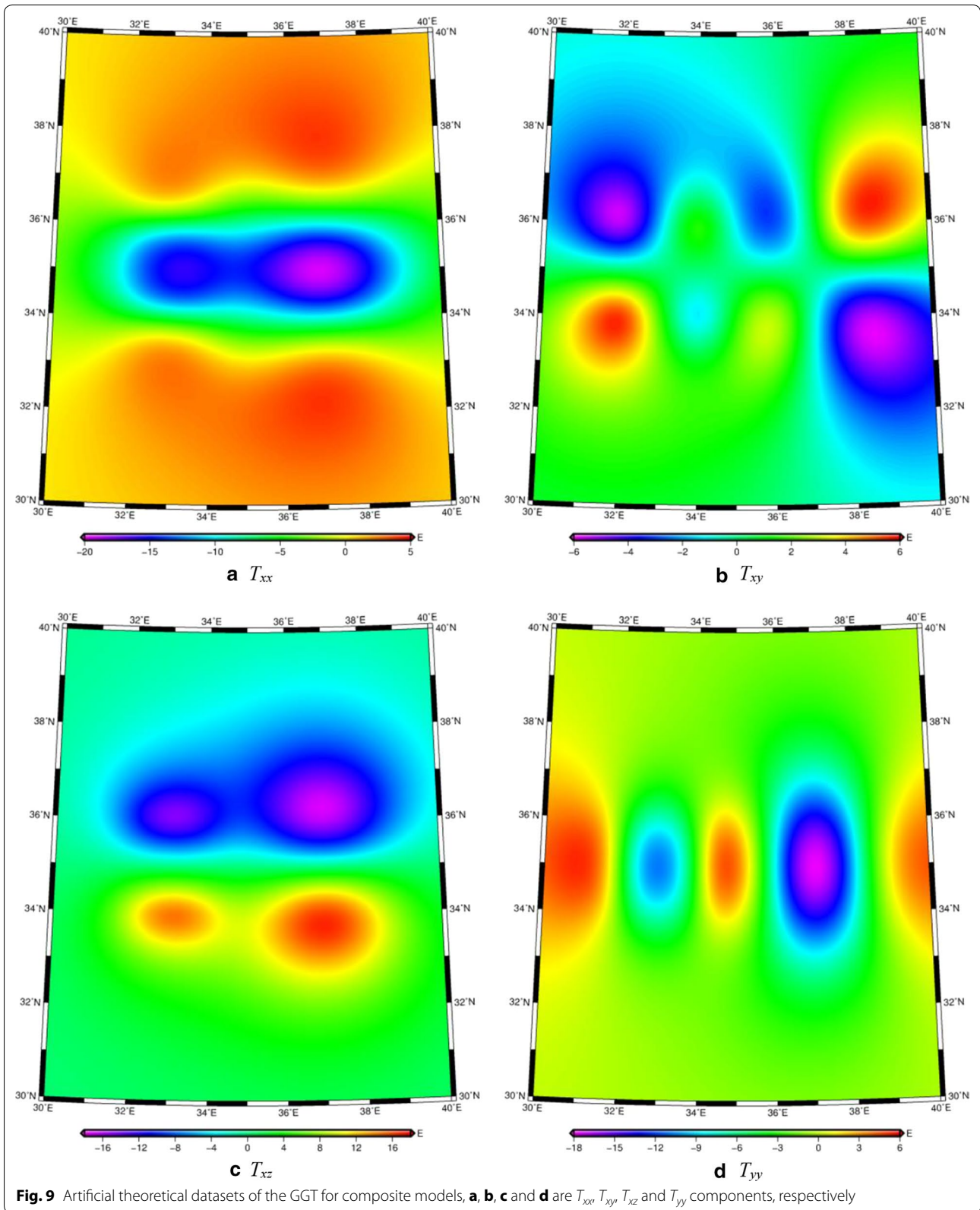
Fig. 8 Artificial synthetic models (two composite models). **a** Horizontal slice of the artificial synthetic model with a radial length of 1698 km, **b** vertical profile of the artificial synthetic model with latitude of 35°

Similarly, we obtained the artificial theoretical datasets of all the components of the GGT (Figs. 9, 10), as well as the added 1% Gaussian random noise, as shown in Figs. 11, 12.

Using the same scheme, with a density bound of 0–0.7 g/cm³, the recovered model was obtained, as in

Fig. 13; the recovered model was well fitted with the blank lines indicating the boundaries of the theoretical models.

Through the artificial theoretical models, we tested our inversion method in the SCS with LNOF. The results indicated that the method is possible to be employed in interior density structure model inversion. In the next



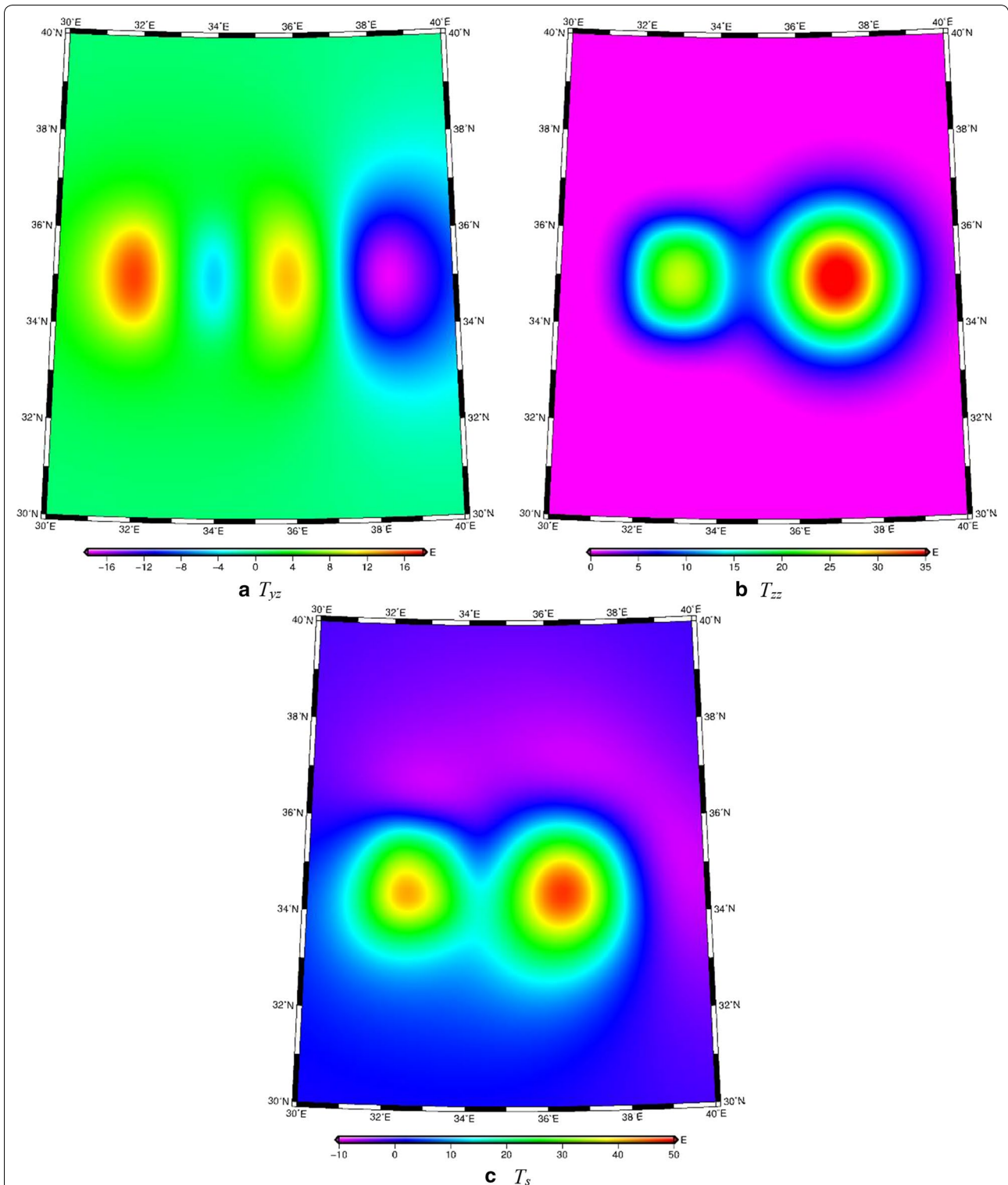


Fig. 10 Artificial theoretical datasets of the GGT for composite models, **a** and **b** are T_{yz} and T_{zz} components of the GGT, respectively, and **c** T_s is the summation of T_{xx} , T_{yy} , T_{zz} , T_{xy} , T_{xz} , T_{yz} and T_{zx}

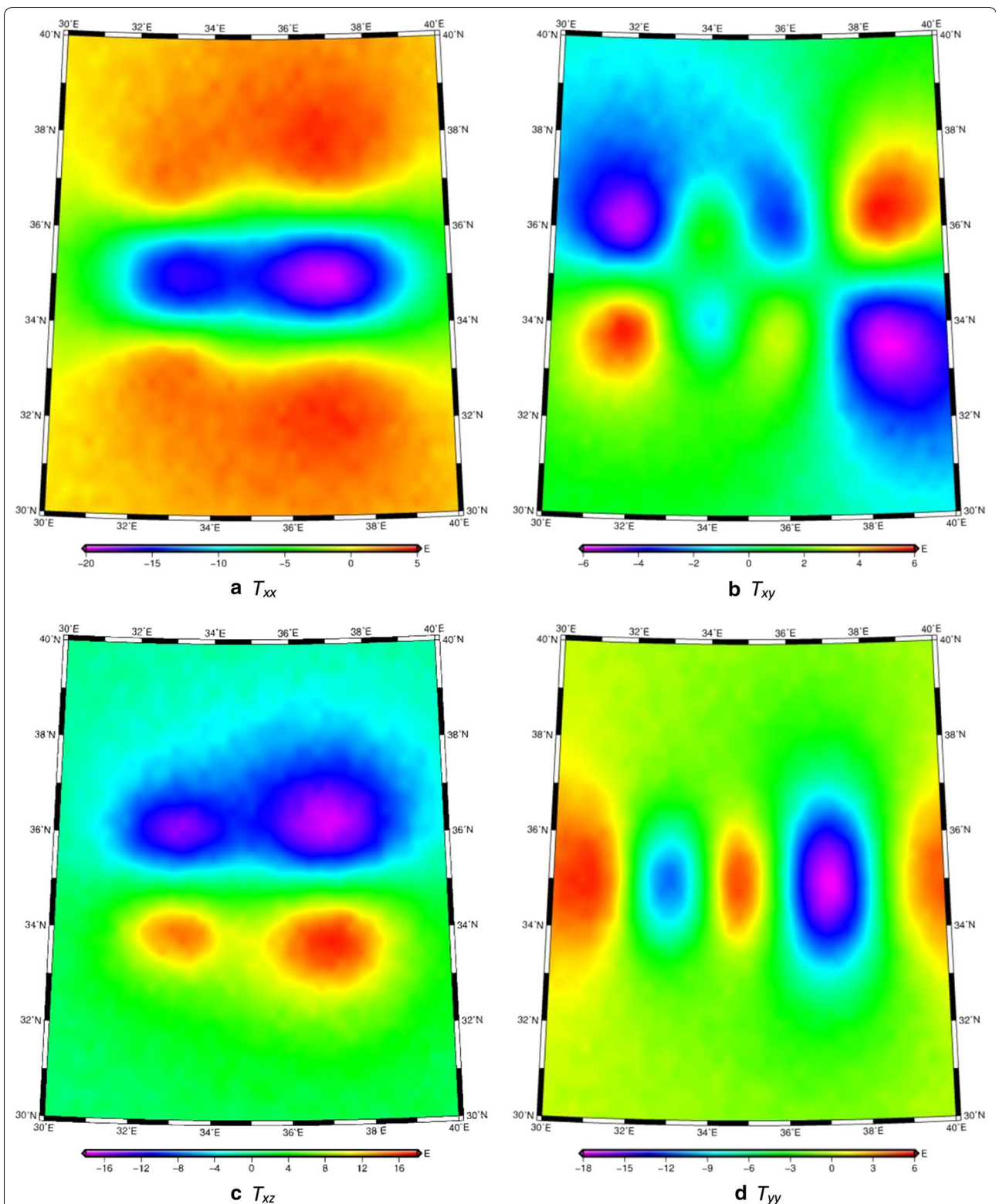


Fig. 11 Artificial theoretical datasets of the GGT with noise for composite models, **a**, **b**, **c** and **d** are T_{xx} , T_{xy} , T_{xz} and T_{yy} component of the GGT, respectively

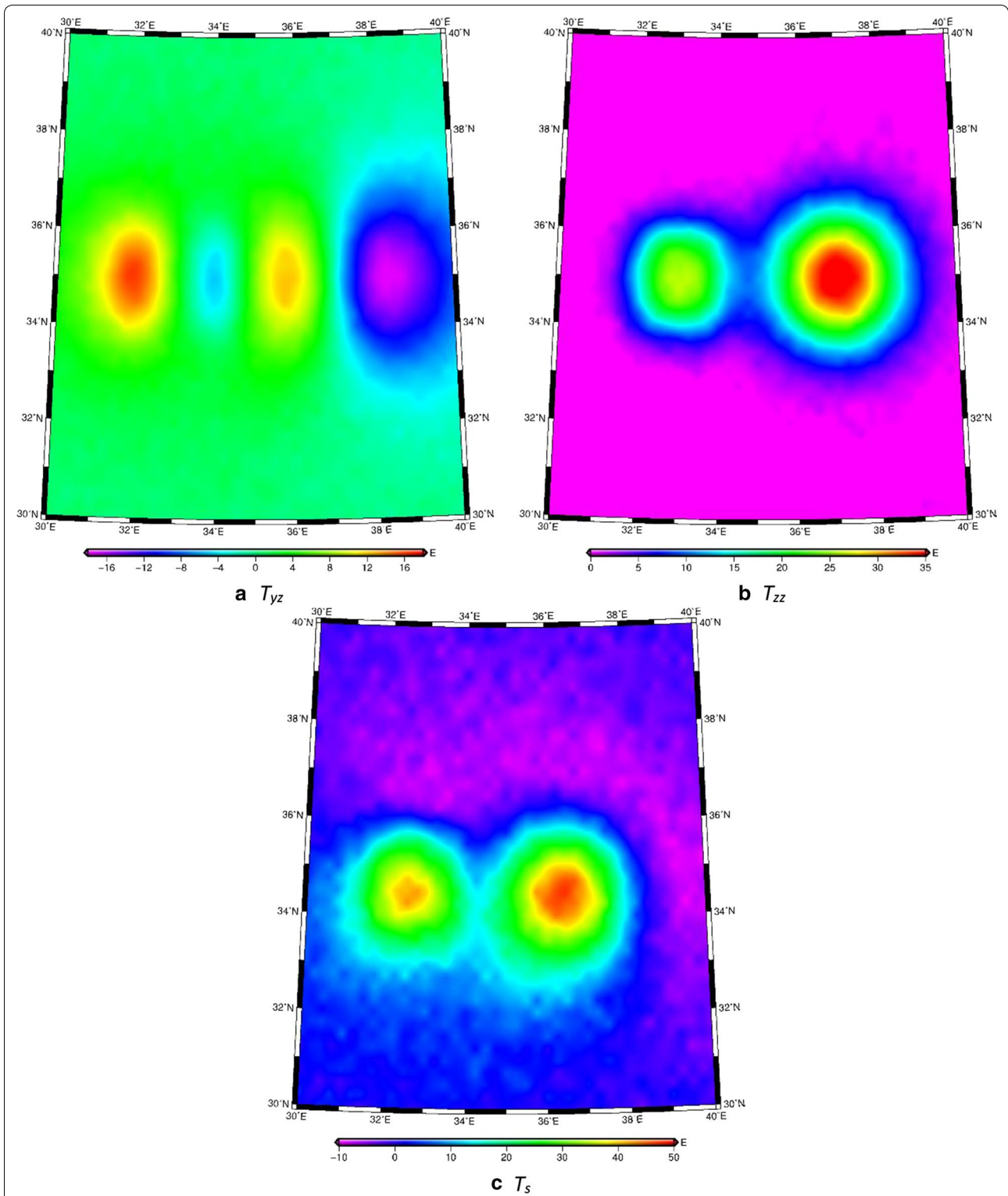


Fig. 12 Artificial theoretical datasets of the GGT with noise for composite models, **a** and **b** are T_{yz} and T_{zz} components of the GGT, respectively, and **c** T_s is the summation of T_{xx} , T_{yy} , T_{zz} , T_{xy} , T_{yz} and T_{zx}

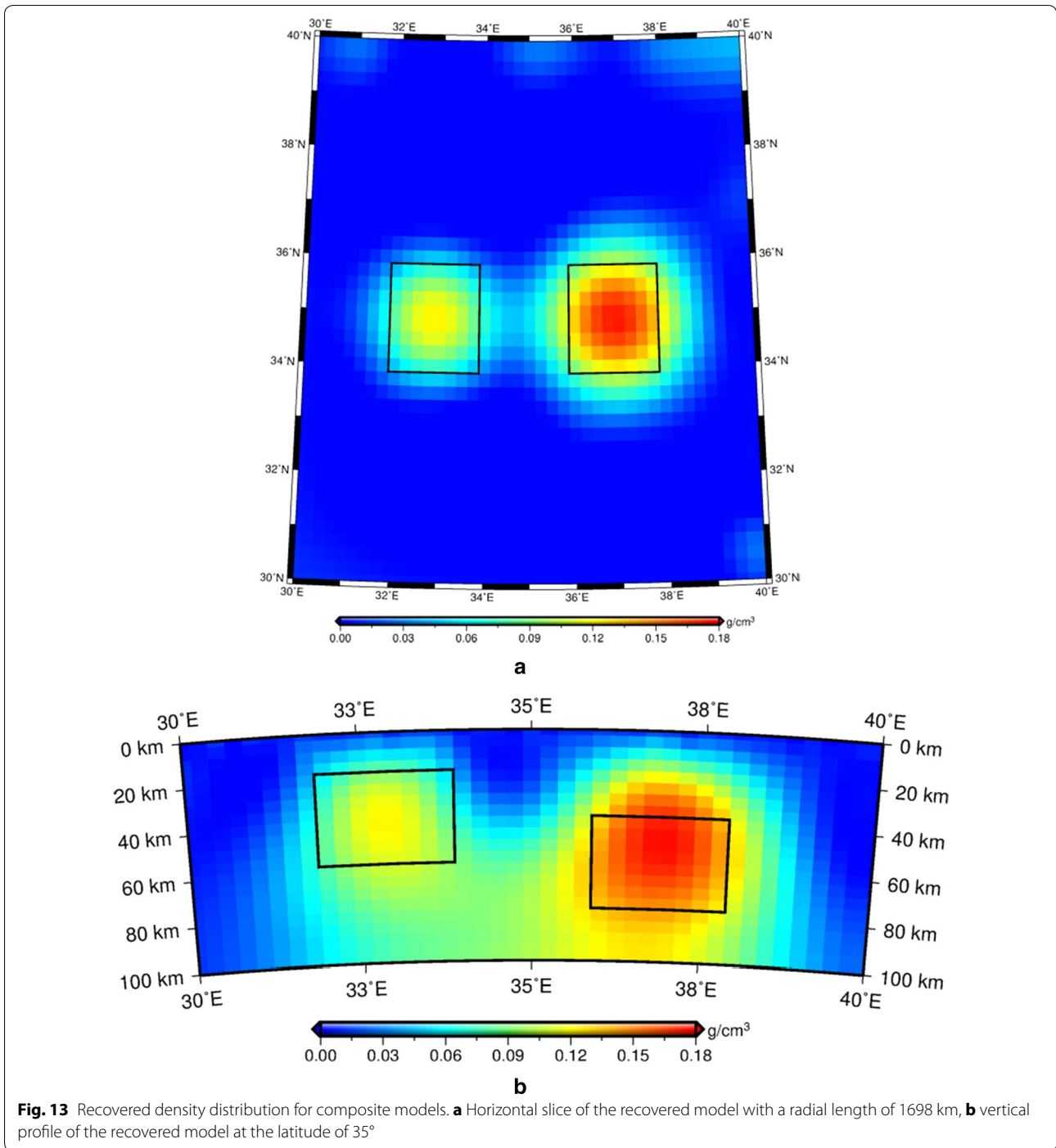
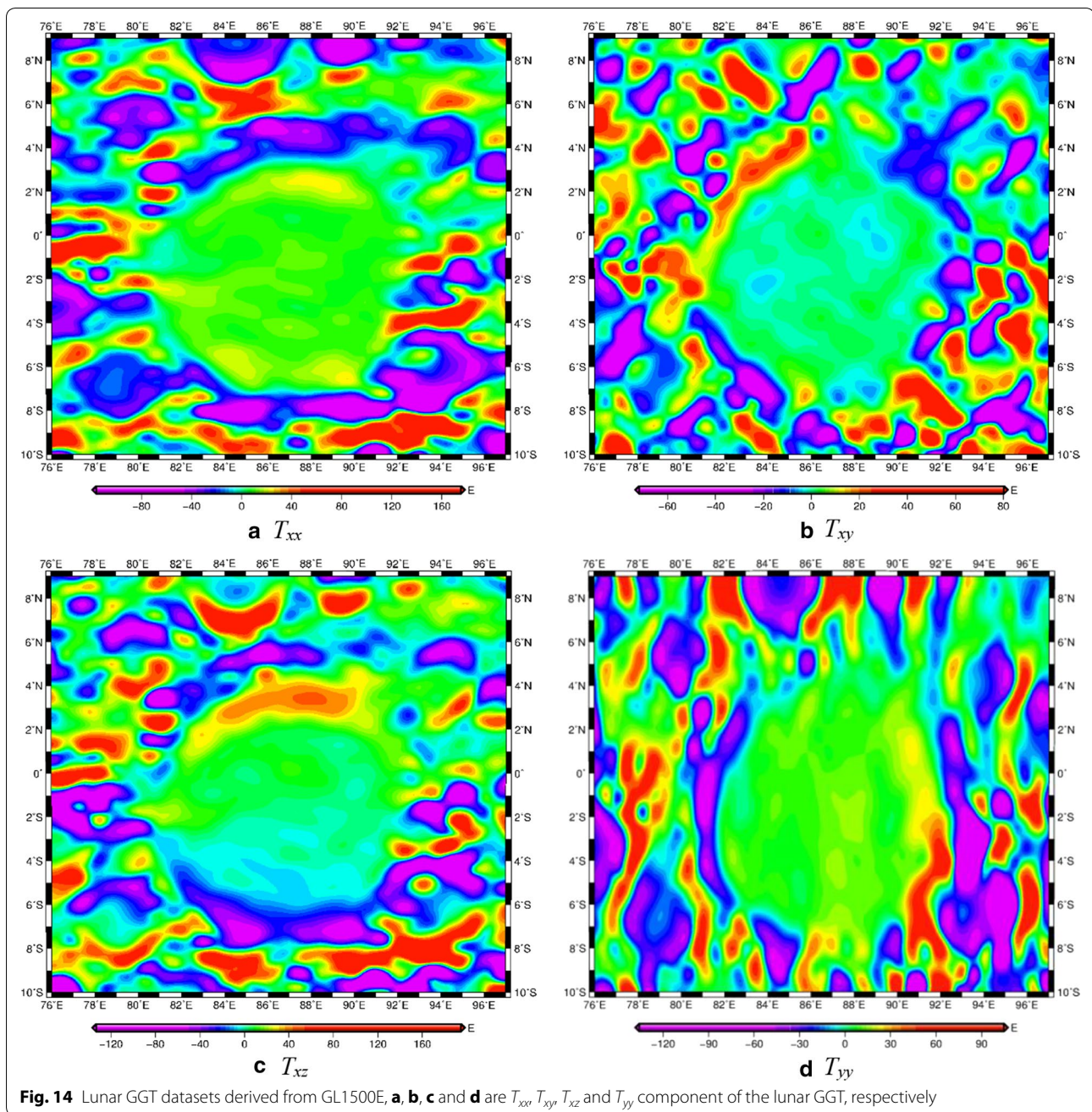


Table 2 3D mesh and datasets for the inversion of Mare Smythii

Direction	Inversion range	Model		Data	
		Grid size	Grid number	Data size	Data number
Longitude	76.0°–97.0°	0.25°	84	0.25°	85
Latitude	–10.0°–9.0°	0.25°	76	0.25°	77
Depth/elevation	0–100 km	5 km	20	0.5 km	

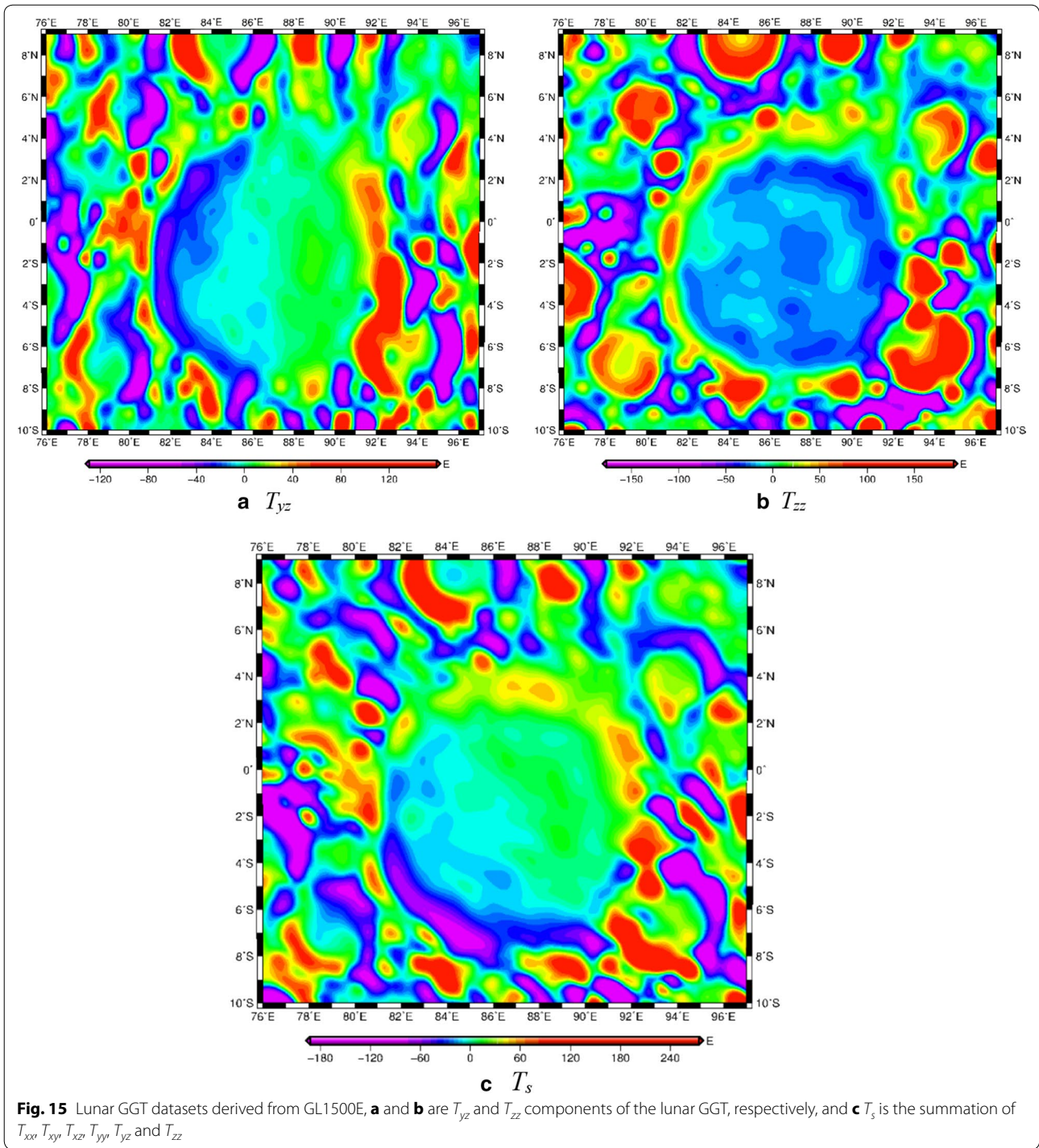


section, we will make use of the actual lunar GGT datasets to validate our inversion method.

Inversion of GGT data at lunar mascon

We selected the Mare Smythii mascon as an example. The Mare Smythii is a lunar mare located along the equator on the easternmost edge of the lunar near side (Wilhelms 1987). According to Liang et al. (2014), our model mesh should have a grid size that approximately equaled to 8 km, i.e., 0.25° by 0.25° on sphere (Table 2),

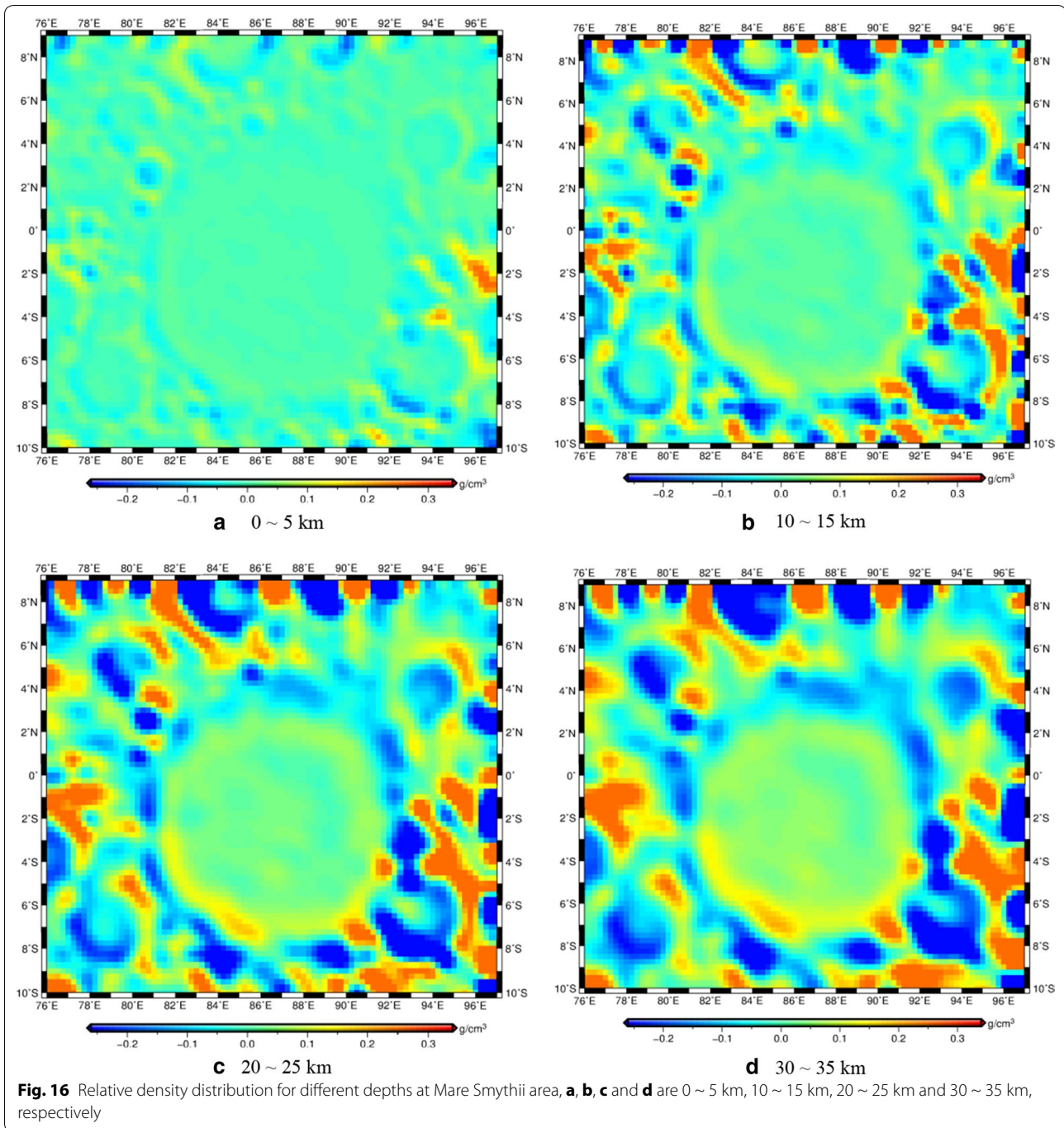
which meant the suitable maximum degree of the lunar gravity model should be 720. Hence, the GGT datasets of this mare derived from lunar gravity field GL1500E with a degree and order up to 720 (The Planetary Data System 2016) are shown in Figs. 14, 15, and the expressions for GGT in LNOF we used came from spherical harmonics (Eshagh 2010). We used a Bouguer correction to remove the gravity effect of the lunar topography and deployed a Gaussian averaging function with an averaging radius of 10 km, which matched the size of the divided cells, to



reduce the leakage errors caused by high-degree spherical harmonic coefficients. Actually, the Gaussian averaging function was proved to be double-edged (Jekeli 1981); if the selected radius was too large, the filter will remove the useful information and the calculated components will be too smooth. In this paper, we preferred to choose

a smaller Gaussian averaging radius which keeps more useful details.

The spherical harmonic coefficients below degree 6 were removed from the GGT datasets we used, and the gravity signal from the left degrees was assumed to be only affected by the lunar crust. The average density of

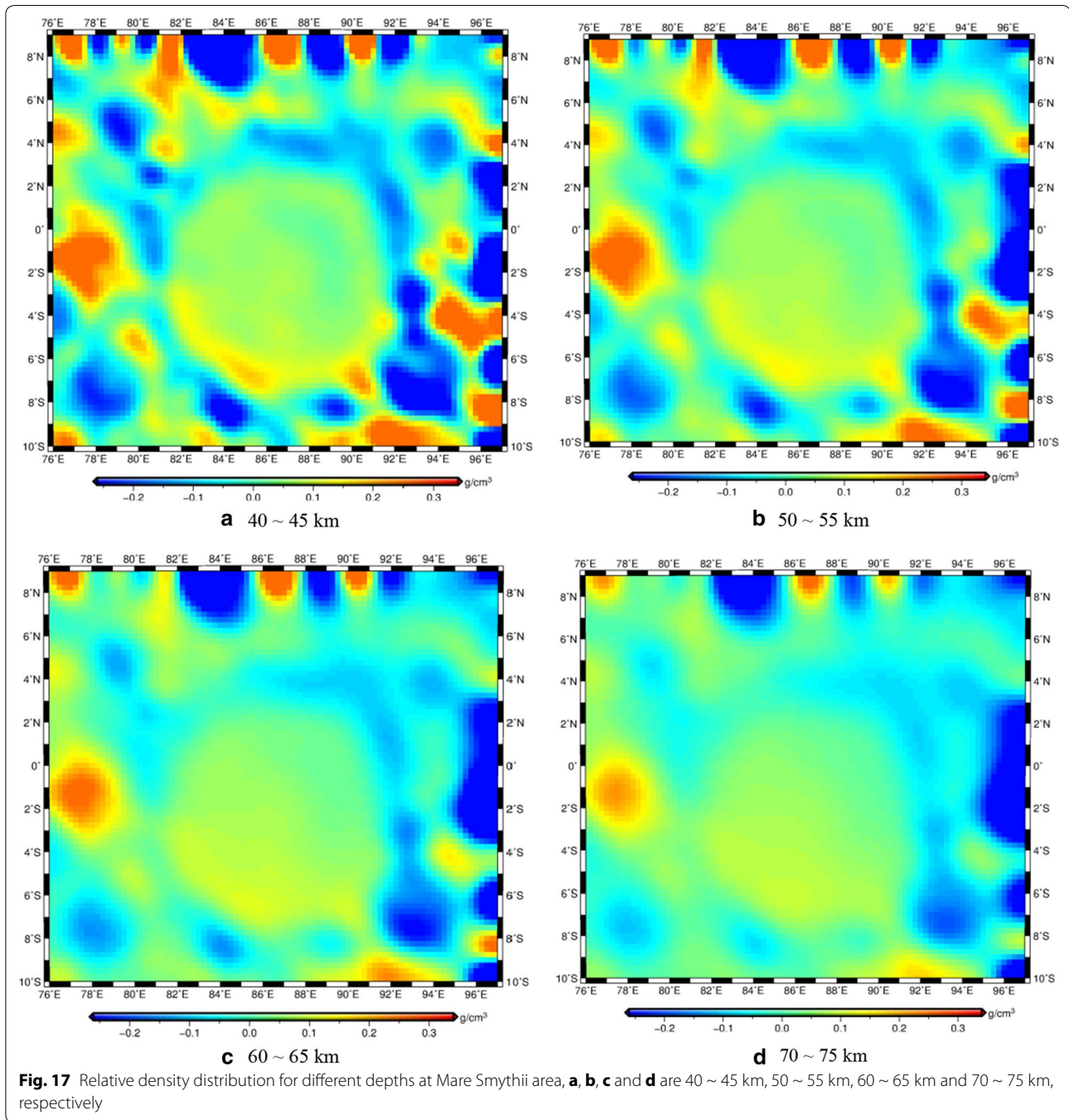


the lunar crust we use here is generally 2.56 g/cm^3 , at a range of $2.30\text{--}2.90 \text{ g/cm}^3$ (Wieczorek et al. 2013). This was also considered as the geological constraint during the inverse process. The 3D mesh and datasets for the inversion of the Mare Smythii are described in Table 2.

By using the GGT datasets as well as the density bounds, we produced an image of the relative density distribution of the Mare Smythii, as shown in Figs. 16, 17

and 18, and the density distribution shows that the depth of Mare Smythii is deeper than which referred from Wieczorek et al. (2013) and similar with the result from Andrews-Hanna et al. (2013).

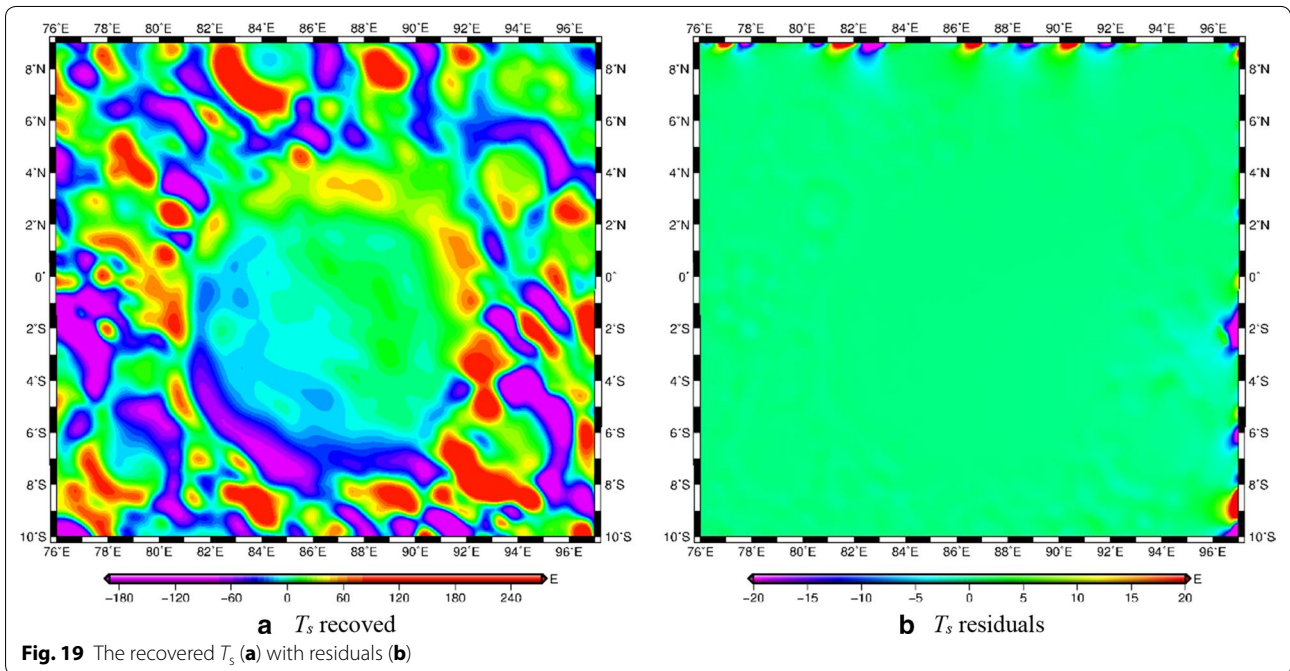
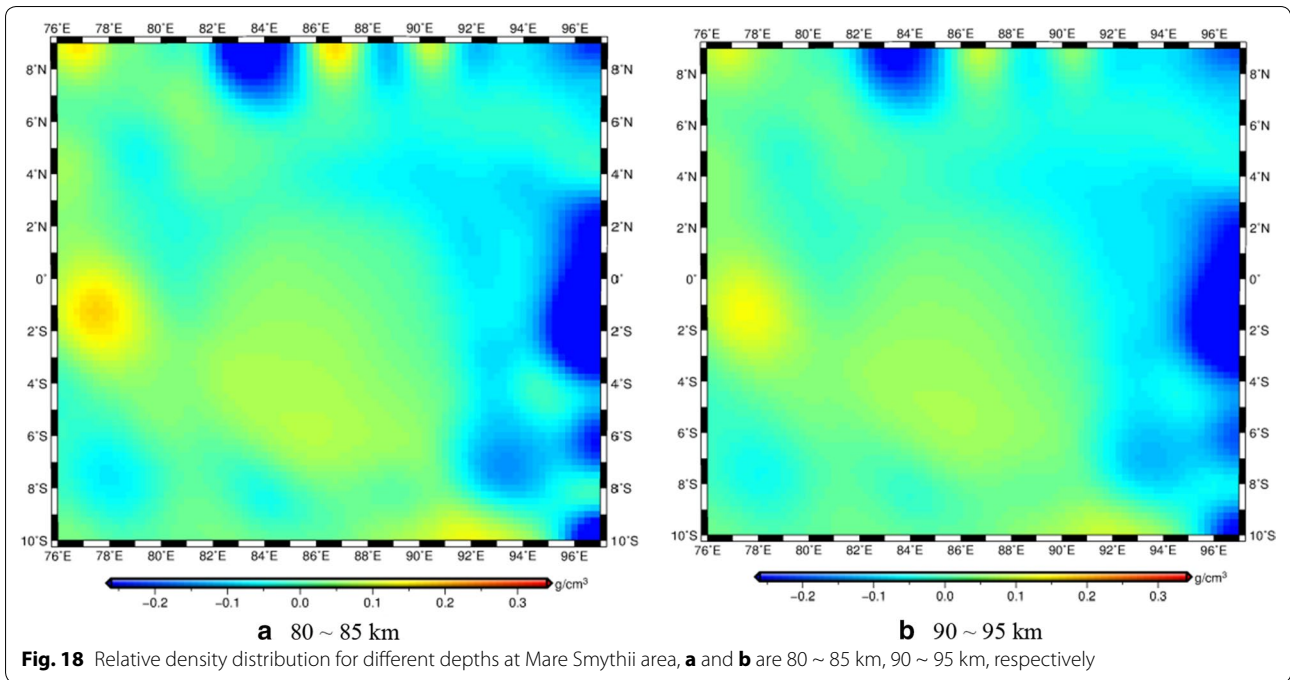
The gravity gradient reflects the density anomaly; Figs. 16, 17 and 18 shows that there are multi-ring structures (Spudis 1993) at the Mare Smythii site. As the density distribution of the Mare Smythii we extracted



through inversion showed some annulus density structures in the shallow stratum and these annulus density structures had the mascon center as the origin point, therefore we infer that there are significant density changes occurred from inside to outside. The formation of these annulus density structures is possibly explained by impacts and crater excavations (Melosh et al. 2013; Montesi 2013). When impacts occur, the kinetic energy is intense and is transformed into heat; this may cause

melting and even vaporize the lunar crust, with cracked lunar crust rocks splashing out of the impact basin. After an impact, a rebalancing of the lunar crust and mantle will likely promote an uplifting of the deeper magma to fill in or eject around an impact basin. The density difference as well as the distance of an ejection could be the reason behind the annulus density structures in this area.

The recovered T_s (Fig. 19a) is similar to the original T_s shown in Fig. 15c and the data residual in Fig. 19b, and



the difference between original T_s and recovered T_s also meets our standard deviation expectation of about 5 E. From Fig. 19b, we can see that the residuals inside the Mare Smythii region are close to zero, and it means the good performance of our inversion method. The random big residual values at the verge are caused by the boundary effects.

Conclusion

An inversion method is fundamental when developing an advanced understanding of the interior structure of planetary geological structures. We presented an effective algorithm that uses full gravity gradient tensor data in spherical coordinate system using local north-oriented frame. In the test case using simulated data, we used two

different models, single and composite models. By checking the differences between the simulated and recovered models, we demonstrated the reliability of our method. We also tested the method on observed data from the Mare Smythii mascon area located on the lunar near side and obtained its interior density distribution. This method could also be applied more generally in magnetic data inversion and in exploratory studies of geological structures of large areas.

Additional file

Additional file 1. Length scale in spherical coordinate system.

Abbreviations

GGT: gravity gradient tensor; SCS: spherical coordinate system; CCS: Cartesian coordinate system; SVD: singular value decomposition; FEM: finite element method; GSF: geocentric spherical frame; LNOF: local north-oriented frame.

Authors' contributions

YZ and JY conceived and designed the experiment; YZ performed the computation; YW analyzed the data; HW interpreted the results; and JAPR and YQ discussed the results and polished the manuscript. YZ and JY wrote the paper, and all the authors improved it. All authors read and approved the final manuscript.

Author details

¹ Key Laboratory of Earthquake Geodesy, Institute of Seismology, China Earthquake Administration, 48 Hongshan Side Road, Wuhan 430071, Hubei, China. ² State Key Laboratory of Engineering in Surveying, Mapping and Remote Sensing, Wuhan University, 129 Luoyu Road, Wuhan 430070, Hubei, China. ³ MOE Key Laboratory of Fundamental Physical Quantities Measurement, School of Physics, Huazhong University of Science and Technology, 1037 Luoyu Road, Wuhan 430074, Hubei, China. ⁴ Hubei Key Laboratory of Gravitation and Quantum Physics, School of Physics, Huazhong University of Science and Technology, 1037 Luoyu Road, Wuhan 430074, Hubei, China. ⁵ Planetary Science Institute, 1700 East Fort Lowell Road, Suite 106, Tucson, AZ 85719-2395, USA. ⁶ DFH Satellite Co. LTD, 104 Youyi Road, Beijing 100094, China.

Acknowledgements

The authors thank Stephen McClure for fruitful and informative discussions.

Competing interests

The authors declare that they have no competing interests.

Data and resources

The source codes for this work can be obtained by contacting the corresponding author. Some of the figures were produced using Generic Mapping Tools (GMT).

Funding

This work is supported by grant of the National Natural Science Foundation of China (41374024, 41704082), Director Foundation of the Institute of Seismology, China Earthquake Administration (IS201616249), Key Laboratory of Geospace Environment and Geodesy, Ministry of Education, Wuhan University (16-01-02), and Hubei Province Natural Science Foundation innovation group Project (2015CFA011).

Publisher's Note

Springer Nature remains neutral with regard to jurisdictional claims in published maps and institutional affiliations.

Received: 15 September 2017 Accepted: 27 March 2018

Published online: 16 April 2018

References

- Anderson EG (1976) The effect of topography on solutions of Stokes' problem, Unisurv S-14, Rep, School of Surveying, University of New South Wales, Kensington
- Andrews-Hanna JC, Asmar SW, Head JW, Kiefer WS, Konopliv AS, Lemoine FG, Matsuyama I, Mazarico E, McGovern PJ, Melosh HJ, Neumann GA, Nimmo F, Phillips RJ, Smith DE, Solomon SC, Taylor GJ, Wicczorek MA, Williams JG, Zuber MT (2013) Ancient igneous intrusions and early expansion of the Moon revealed by GRAIL gravity gradiometry. *Science* 339:675–678. <https://doi.org/10.1126/science.1231753>
- Andrews-Hanna JC, Besserer J, Head JW III, Howett CJA, Kiefer WS, Lucey PJ, McGovern PJ, Melosh HJ, Neumann GA, Phillips RJ, Schenk PM, Smith DE, Solomon SC, Zuber MT (2014) Structure and evolution of the lunar Procellarum region as revealed by GRAIL gravity data. *Nature* 514:68–71. <https://doi.org/10.1038/nature13697>
- Asgharzadeh MF, von Frese RRB, Kim HR, Leftwich TE, Kim JW (2007) Spherical prism gravity effects by Gauss–Legendre quadrature integration. *Geophys J Int* 169:1–11. <https://doi.org/10.1111/j.1365-246X.2007.03214.x>
- Backus G, Gilbert J (1967) Numerical applications of a formalism for geophysical inverse problems. *Geophys J R Astron Soc* 13:247–276. <https://doi.org/10.1111/j.1365-246X.1967.tb02159.x>
- Backus G, Gilbert F (1968) The resolving power of gross Earth data. *Geophys J R Astron Soc* 16:169–205. <https://doi.org/10.1111/j.1365-246X.1968.tb00216.x>
- Backus G, Gilbert F (1970) Uniqueness in the inversion of inaccurate gross Earth data. *Philos Trans R Soc Lond Ser A Math Phys Sci* 266:123–192
- Barbosa V, Silva J (1994) Generalized compact gravity inversion. *Geophysics* 59:57–68. <https://doi.org/10.1190/1.1443534>
- Bell R, Hansen R (1998) The rise and fall of early oil field technology: the torsion balance gradiometer. *Lead Edge* 17:81–83. <https://doi.org/10.1190/1.1437836>
- Bouman J, Ebbing J, Fuchs M, Sebera J, Lieb V, Szwillus W, Haagmans R, Novak P (2016) Satellite gravity gradient grids for geophysics. *Sci Rep* 6:21050. <https://doi.org/10.1038/srep21050>
- Calvetti D, Morigi S, Reichel L, Sgallari F (2000) Tikhonov regularization and the L-curve for large discrete ill-posed problems. *J Comput Appl Math* 123:423–446. [https://doi.org/10.1016/S0377-0427\(00\)00414-3](https://doi.org/10.1016/S0377-0427(00)00414-3)
- Capriotti J, Li Y, Krahenbuhl R (2015) Joint inversion of gravity and gravity gradient data using a binary formulation. In: International workshop and gravity, electrical & magnetic methods and their applications, Chenghu, China, 19–22 April 2015. Society of Exploration Geophysicists and Chinese Geophysical Society, pp 326–329. <https://doi.org/10.1190/gem2015-085>
- Eshagh M (2008) Non-singular expressions for the vector and the gradient tensor of gravitation in a geocentric spherical frame. *Comput Geosci* 34:1762–1768. <https://doi.org/10.1016/j.cageo.2008.02.022>
- Eshagh M (2010) Alternative expressions for gravity gradients in local north-oriented frame and tensor spherical harmonics. *Acta Geophys* 58:215–243. <https://doi.org/10.2478/s11600-009-0048-z>
- Farquharson CG (2008) Constructing piecewise-constant models in multidimensional minimum-structure inversions. *Geophysics* 73:K1–K9. <https://doi.org/10.1190/1.2816650>
- Freed AM, Johnson BC, Blair DM et al (2014) The formation of lunar mascon basins from impact to contemporary form. *J Geophys Res (Planets)* 119:2378–2397. <https://doi.org/10.1002/2014JE004657>
- Geng M, Yang Q, Huang D (2015) 3D joint inversion of gravity-gradient and borehole gravity data. *Explor Geophys* 48:151–165. <https://doi.org/10.1071/EG15023>
- Guillen A, Menichetti V (1984) Gravity and magnetic inversion with minimization of a specific functional. *Geophysics* 49:1354–1360. <https://doi.org/10.1190/1.1441761>
- Heck B, Seitz K (2007) A comparison of the tesseroïd, prism and point-mass approaches for mass reductions in gravity field modeling. *J Geod* 81:121–136. <https://doi.org/10.1007/s00190-006-0094-0>
- Jansen JC, Andrews-Hanna JC, Li Y et al (2017) Small-scale density variations in the lunar crust revealed by GRAIL. *Icarus* 291:107–123. <https://doi.org/10.1016/j.icarus.2017.03.017>
- Jekeli C (1981) Alternative methods to smooth the Earth's gravity field. NASA technical report
- Last B, Kubik K (1983) Compact gravity inversion. *Geophysics* 48:713–721. <https://doi.org/10.1190/1.1441501>

- Li Y (2001) 3-D inversion of gravity gradiometer data. In SEG technical program expanded abstracts 2001; SEG technical program expanded abstracts; society of exploration geophysicists, pp 1470–1473
- Li Y, Oldenburg D (1996) 3-D inversion of magnetic data. *Geophysics* 61:394–408. <https://doi.org/10.1190/1.1443968>
- Li Y, Oldenburg D (1998) 3-D inversion of gravity data. *Geophysics* 63:109–119. <https://doi.org/10.1190/1.1444302>
- Liang Q, Chen C, Li Y (2014) 3-D inversion of gravity data in spherical coordinates with application to the GRAIL data. *J Geophys Res (Planets)* 119:1359–1373. <https://doi.org/10.1002/2014JE004626>
- Martinez C, Li Y, Krahenbuhl R, Braga MA (2012) 3D inversion of airborne gravity gradiometry data in mineral exploration: a case study in the Quadrilátero Ferrífero, Brazil. *Geophysics* 78:B1–B11. <https://doi.org/10.1190/geo2012-0106.1>
- Matsumoto K, Goossens S, Ishihara Y et al (2010) An improved lunar gravity field model from SELENE and historical tracking data: revealing the farside gravity feature. *J Geophys Res*. <https://doi.org/10.1029/2009JE003499>
- Melosh HJ, Freed AM, Johnson BC et al (2013) The origin of Lunar mascon basins. *Science* 340:1552–1555. <https://doi.org/10.1126/science.1235768>
- Meng Z (2016) 3D inversion of full gravity gradient tensor data using SLO sparse recovery. *J Appl Geophys* 127:112–128. <https://doi.org/10.1016/j.jappgeo.2016.02.010>
- Montesi LGJ (2013) Solving the mascon mystery. *Science* 340:1535–1536. <https://doi.org/10.1126/science.1238099>
- Muller PM, Sjogren WL (1968) Mascons: Lunar mass concentrations. *Science* 161:680–684. <https://doi.org/10.1126/science.161.3842.680>
- Oldenburg D, Li Y (2005) Inversion for applied geophysics: a tutorial. In: Near-surface geophysics. Society of exploration geophysicists, pp 89–150
- Oliveira VC, Barbosa VCF (2013) 3-D radial gravity gradient inversion. *Geophys J Int* 195(2):883–902
- Paoletti V, Fedi M, Italiano F, Florio G, Ialongo S (2016) Inversion of gravity gradient tensor data: does it provide better resolution? *Geophys J Int* 205:192–202. <https://doi.org/10.1093/gji/ggw003>
- Pedersen LB, Rasmussen TM (1990) The gradient tensor of potential field anomalies: some implications on data collection and data processing of maps. *Geophysics* 55:1558–1566. <https://doi.org/10.1190/1.1442807>
- Petrovskaya MS, Vershkov AN (2006) Non-singular expressions for the gravity gradients in the local north-oriented and orbital reference frames. *J Geod* 80:117–127. <https://doi.org/10.1007/s00190-006-0031-2>
- Pilkington M (2012) Analysis of gravity gradiometer inverse problems using optimal design measures. *Geophysics* 77:G25–G31. <https://doi.org/10.1190/geo2011-0317.1>
- Pilkington M (2013) Evaluating the utility of gravity gradient tensor components. *Geophysics* 79:G1–G14. <https://doi.org/10.1190/geo2013-0130.1>
- Reed GB (1973) Application of kinematical geodesy for determining the short wave length components of the gravity field by satellite gradiometry, Ohio State University
- Spudis PD (1993) The geology of multi-ring impact basins. Cambridge University Press
- Sun J, Li Y (2014) Adaptive Lp inversion for simultaneous recovery of both blocky and smooth features in a geophysical model. *Geophys J Int* 197:882–899. <https://doi.org/10.1093/gji/ggu067>
- The Planetary Data System (2016) GRAIL Moon LGRS derived gravity science data products V1.0
- Tikhonov AN, Arsenin VY (1977) Solution of ill-posed problems. W. H. Winston & Sons Inc, Washington
- Uieda L, Barbosa VCF (2012) Robust 3D gravity gradient inversion by planting anomalous densities. *Geophysics* 77:G55–G66. <https://doi.org/10.1190/geo2011-0388.1>
- Vasco DW (1989) Resolution and variance operators of gravity and gravity gradiometry. *Geophysics* 54:889–899. <https://doi.org/10.1190/1.1442717>
- Vasco D, Taylor C (1991) Inversion of airborne gravity gradient data, southwestern Oklahoma. *Geophysics* 56:90–101. <https://doi.org/10.1190/1.1442961>
- Wang X, Liang Q, Chao C et al (2015) Crust-mantle structure beneath the sinus iridium mare imbrium basin of the Moon. *Earth Sci* 40:1566–1575. <https://doi.org/10.3799/dqkx.2015.141>
- Wieczorek MA, Neumann GA, Nimmo F, Kiefer WS, Taylor GJ, Melosh HJ, Phillips RJ, Solomon SC, Andrews-Hanna JC, Asmar SW, Konopliv AS, Lemoine FG, Smith DE, Watkins MM, Williams JG, Zuber MT (2013) The crust of the Moon as seen by GRAIL. *Science* 339:671–675. <https://doi.org/10.1126/science.1231530>
- Wilhelms DE (1987) Geologic history of the Moon, US Geological Survey professional paper 1348
- Williams NC (2008) Geologically-constrained UBC-GIF gravity and magnetic inversions with examples from the Agnew-Wiluna greenstone belt, Western Australia. University of British Columbia. <https://doi.org/10.14288/1.0052390>
- Yan J, Goossens S, Matsumoto K et al (2012) CEGM02: an improved lunar gravity model using Chang'E-1 orbital tracking data. *Planet Space Sci* 62:1–9. <https://doi.org/10.1016/j.pss.2011.11.010>
- Zhang Y, Yan J, Li F, Chen C, Mei B, Jin S, Dohm JH (2015) A new bound constraints method for 3-D potential field data inversion using Lagrangian multipliers. *Geophys J Int* 201:267–275. <https://doi.org/10.1093/gji/ggv016>
- Zhdanov MS, Ellis R, Mukherjee S (2004) Three-dimensional regularized focusing inversion of gravity gradient tensor component data. *Geophysics* 69:925–937. <https://doi.org/10.1190/1.1778236>
- Zuber MT, Smith DE, Lehman DH, Hoffman TL, Asmar SW, Watkins MM (2013a) Gravity Recovery and Interior Laboratory (GRAIL): mapping the lunar interior from crust to core. *Space Sci Rev* 178:3–24. <https://doi.org/10.1007/s11214-012-9952-7>
- Zuber MT, Smith DE, Watkins MM, Asmar SW, Konopliv AS, Lemoine FG, Melosh HJ, Neumann GA, Phillips RJ, Solomon SC, Wieczorek MA, Williams JG, Goossens SJ, Kruizinga G, Mazarico E, Park RS, Yuan DN (2013b) Gravity Field of the Moon from the Gravity Recovery and Interior Laboratory (GRAIL) mission. *Science* 339:668–671. <https://doi.org/10.1126/science.1231507>

Submit your manuscript to a SpringerOpen® journal and benefit from:

- Convenient online submission
- Rigorous peer review
- Open access: articles freely available online
- High visibility within the field
- Retaining the copyright to your article

Submit your next manuscript at ► springeropen.com